Editors' Suggestion

Effects of Long- and Short-Range Ferroelectric Order on the Electrocaloric Effect in Relaxor Ferroelectric Ceramics

Junjie Li,[1,2] Jianting Li,[1,2] Shiqiang Qin,[1,2] Xiaopo Su,[1,2] Lijie Qiao,[1,2] Yu Wang,[3] Turab Lookman,[4]
and Yang Bai[1,2,*]

[1] *Beijing Advanced Innovation Center for Materials Genome Engineering, University of Science and Technology Beijing, Beijing 100083, China*
[2] *Key Laboratory of Environmental Fracture (Ministry of Education), University of Science and Technology Beijing, Beijing 100083, China*
[3] *School of Materials Science and Engineering, Nanchang University, Nanchang 330031, Jiangxi, China*
[4] *Theoretical Division, Los Alamos National Laboratory, Los Alamos, New Mexico 87545, USA*

(Received 9 October 2018; revised manuscript received 6 January 2019; published 11 April 2019)

We study the electrocaloric effect (ECE) in a typical relaxor ferroelectric ceramic of $Pb_{0.91}La_{0.06}Zr_{0.8}Ti_{0.2}O_3$ by analyzing the respective contributions of long-range-ordered ferroelectric macrodomains and short-range-ordered polar nanoregions (PNRs) by both direct and indirect characterization. The ECE exhibits two peaks in its dependence on temperature, the former responds to the transition from long-range ferroelectric order to short-range-ordered PNRs and the latter likely to the transition between two kinds of PNRs with different phase structures or motion states. The contributions of different mechanisms are clarified by resolving the overlapping peaks in direct heat flow experimental results. The first peak has a $\Delta T_{\max} = 0.7$ K at 80 °C (approximately T_d) and the second a $\Delta T_{\max} = 0.98$ K at 140 °C (approximately T_m) under 40 kV/cm. We conclude that the thermodynamic method based on the Maxwell relation is not applicable if PNRs are involved as their signatures are only picked up by direct measurements, but is valid for the case of ferroelectric domain rotation or phase transition where it provides a reasonably accurate ECE result. Besides the impact on aspects related to metrology, our work suggests that the region between the peaks in ΔT-T curves may be used to produce a large electrocaloric ΔT over a broad temperature range, which is highly desirable in cooling applications.

DOI: 10.1103/PhysRevApplied.11.044032

I. INTRODUCTION

Heat-generating devices have played a key role in the development and progress of modern society so that today, small devices are used in electronic chips and large ones are employed in engines, making refrigeration and cooling technologies necessary for their efficient operation. However, most refrigerators are based on the mechanical vapor-compression cycle, with its own series of weaknesses, such as low efficiency, the production of fluorinated greenhouse gases, and nonminiaturization. Recently, ferroelectric refrigeration based on the electrocaloric effect (ECE) has shown promise as a prospective cooling technology [1–5].

The ECE is a basic physical phenomenon in ferroelectric dipolar systems, where the change of an external electric field (ΔE) induces reversible isothermal entropy change (ΔS) and/or adiabatic temperature change (ΔT). Since a giant ΔT of up to 12 K was successively obtained in inorganic and organic thin films in 2006 and 2008 [1,2], electrocalorics have become the center of much interest within the ferroelectric community in the recent decade [6,7], and are widely studied in various ferroelectric materials, including single crystals [8–10], ceramics [11–13], thick films [14–16], and thin films [17–19]. Moreover, an ECE cooling device with a high specific cooling power and a high coefficient of performance was fabricated in 2017, demonstrating the potential for future applications [3].

As reported, the ECE is significantly enhanced near the Curie temperature due to the first-order phase transition from ferroelectric to paraelectric state [1,8], but the narrow working temperature range of the transition does not favor practical applications. This sets a significant challenge for ECE researchers, which is to obtain large ECEs in a wide temperature range. Hence, most attention has focused on relaxor ferroelectrics since in contrast to normal ferroelectrics, relaxor ferroelectrics display a diffused phase transition (DPT) with polar nanoregions (PNRs), which may endow a large ECE temperature change with good temperature stability [20–23]. Although a large amount

---

[*] baiy@mater.ustb.edu.cn

of work has been carried out on various relaxor ferroelectrics, especially around the morphotropic phase boundary (MPB), the effect of PNRs on ECE is still far from clear. The indirect thermodynamic method based on the Maxwell relation, which is used in most ECE research, presents a rather confusing description for relaxor ferroelectrics. The PNRs, giving rise to short-range order, were thought to not contribute to the macroscopic polarization. However, their rearrangement along electric fields or leading to long-range-order ferroelectric microdomains under the action of external electric fields can lead to a large entropy change. In many reports, the entropy change induced by the evolution of PNRs is not considered in the indirect thermodynamic method so that the calculated ECE temperature change is much smaller than the directly measured value [20,24–26]. On the other hand, other studies on typical relaxor ferroelectrics, such as $0.94Na_{1/2}Bi_{1/2}TiO_3$-$0.06BaTiO_3$ and $0.88Pb(Mg_{1/3}Nb_{2/3})O_3$-$0.12PbTiO_3$, find that the indirectly calculated ECE values are more than twice the directly measured data [27,28]. Thus, this paper addresses the need for a clearer understanding of PNRs, especially with regard to the applicability of the Maxwell relation, as the less than clear results obtained by indirect characterization hinder ECE research on relaxor ferroelectrics. We demonstrate how the respective contributions associated with long-range-ordered ferroelectric macrodomains and short-range-ordered PNRs on the ECE arise in a typical relaxor ferroelectric material, namely, $Pb_{0.91}La_{0.06}Zr_{0.8}Ti_{0.2}O_3$ (denoted as PLZT) ceramics, the physics of which is associated with nonergodic and ergodic states in the measurable temperature range. In particular, our work clarifies not only how the structural phase transition can induce an ECE peak, but also how the transitions between short-range PNRs and the long-range ferroelectric phase or even two kinds of PNRs influence the ECE peak. Moreover, the PNRs lead to ΔT vs T curves that show a "platform" between the two peaks at T_d, the depolarization temperature, and T_m, the temperature at which the permittivity is a maximum at low frequency. This is in contrast to the valley between two structural phase transitions, which occurs for normal ferroelectrics. The platform between T_d and T_m has implications for applications as it can allow for a large electrocaloric ΔT over a board temperature range. This is highly desirable for cooling and implies that ECE materials may be designed by using relaxor ferroelectrics with a large T_m-T_d.

II. EXPERIMENT

A. Preparation of PLZT bulk ceramics

The PLZT samples are fabricated using the conventional solid-state reaction method. All raw powders of PbO [analytical reagent (AR), ≥99.0%], La_2O_3 (99.99%), ZrO_2 (AR, ≥99.0%) and TiO_2 (chemical pure, ≥98.0%) are purchased from Sinopharm Chemical Reagent Co. Ltd., China. 5 mol. % excess PbO is added to compensate for the Pb volatilization loss during calcination and sintering [29,30]. After being ground in ethanol for 4 h using a planetary ball mill, the dried mixtures are calcined at 900 °C for 4 h twice for compositional homogeneity. For refining the grain size, the calcined powders are reground in the ball mill. The dried powders are mixed with 5 wt. % polyvinyl alcohol (PVA) solution and pressed into pellets with a diameter of 10 mm and a thickness of 1 mm under 6 MPa pressure. The pellets are sintered at 1300 °C for 3 h in air using a double crucible configuration with homologous and protective PLZT powders. Some samples are poled for 10 min under a dc electric field of 20 kV/cm, while the others are kept in the unpoled state.

B. Characterization

The phase composition of the PLZT ceramic samples is characterized by using an x-ray diffractometer (XRD, Rigaku SmartLab, Japan) at 40 kV and 150 mA with Cu $K\alpha_{1/2}$ radiation. The microstructure of the samples is observed by employing a scanning electron microscope (SEM, JSM-6700F, Japan). The mass density is measured using the Archimedes' drainage method. The specific heat capacity is measured by differential scanning calorimeter (DSC, TA Instruments Q2000, US) with modulated DSC mode (heating rate 2 °C/min, modulation period 100 s, and modulation amplitude 0.8 °C). The Raman spectra are recorded by a high-resolution Raman spectrometer (HORIBA, France). The temperature dependences of dielectric properties are measured with an *LCR* meter (Keysight E4980A, US) equipped with an automated temperature controller at heating ramp rates of 3 °C/min. The dielectric frequency spectra under different temperatures are detected with an impedance analyzer (Keysight E4990A, US) equipped with a temperature chamber. For the high electric field measurements, the sintered ceramic pellets are ground to a final thickness of about 200–300 μm and coated with Ag electrode on both sides. The ferroelectric hysteresis loops are measured at 1 Hz at different temperatures using a ferroelectric analyzer (aixACCT TF2000, Germany). The direct ECE measurements are performed with a modified DSC (TA Instruments Q2000, US).

III. RESULTS AND DISCUSSION

A. Relaxation behavior

Figure 1(a) shows the temperature dependence of the reversible heat capacity in a heating process. The gentle heat capacity peak near 123 °C indicates the feature of DPT. Figure 1(b) shows the temperature dependence of the dielectric constant and loss tangent under different frequencies. A clear frequency dispersion is observed below T_m (133 °C), which also indicates the relaxor characteristics induced by PNRs. Further study on the relaxor

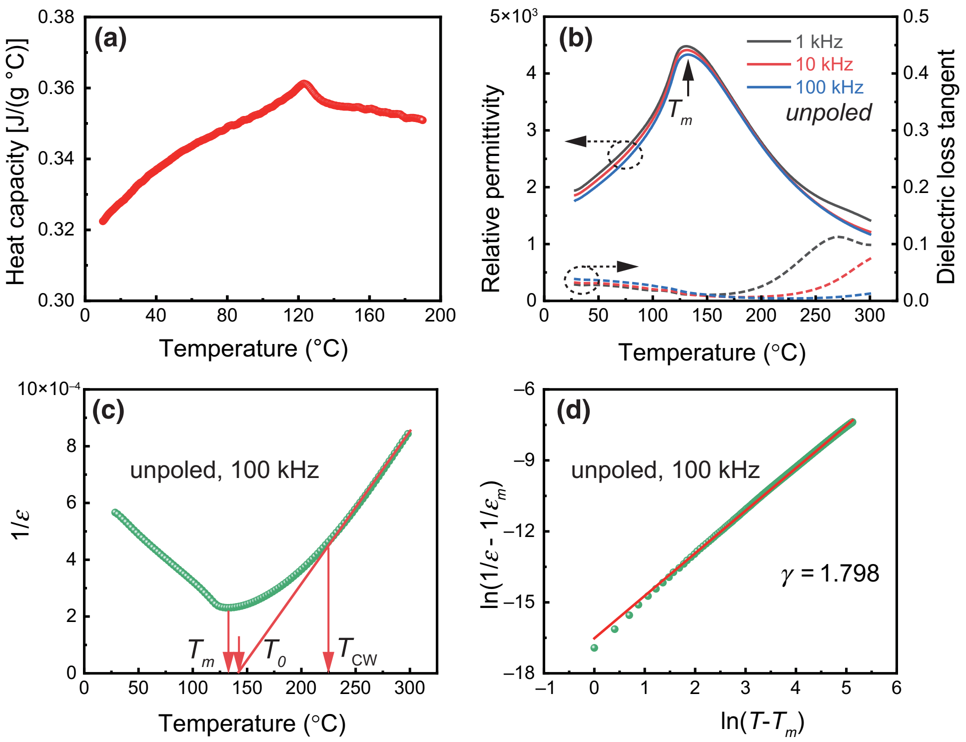

FIG. 1. (a) Temperature dependence of reversible specific heat curve. (b) Temperature-dependent relative permittivity (ε) and loss tangent for ceramic during heating process under different frequencies. (c) The reciprocal of dielectric permittivity ($1/\varepsilon$) as a function of temperature at 100 kHz. The green symbols represent experimental data, whereas the red solid line is the fitting curve by Eq. (1). (d) The plot (green symbols) and linear fitting curve (red solid line) of ln($1/\varepsilon$-$1/\varepsilon_m$) as a function of ln(T-T_m).

characteristics is conducted with reference to the Curie-Weiss law

$$\varepsilon = \frac{C}{T - T_{\mathrm{CW}}} \quad (T > T_{\mathrm{CW}}), \tag{1}$$

where T_{CW} is the Curie–Weiss temperature and C is the Curie–Weiss constant. In contrast to normal ferroelectrics for which T_{CW} is close to T_C, relaxor ferroelectrics have T_{CW} above T_C [31,32]. Figure 1(c) displays the reciprocal of dielectric permittivity ($1/\varepsilon$) vs temperature at 100 kHz. The separation, that is, $\mathrm{T_{CW}}$, appears near 225 °C, which is 92 °C higher than T_m, indicating the rapid growth of dynamic PNRs in PLZT relaxors. Then, a modified Curie–Weiss law can be used to quantitatively describe the diffusive degree of a DPT [21,31,32]

$$\frac{1}{\varepsilon} - \frac{1}{\varepsilon_m} = \frac{(T - T_m)^{\gamma}}{C} \quad (1 \le \gamma \le 2), \tag{2}$$

where γ is the diffusion exponent. As shown in Fig. 1(d), the linear fitting between ln($1/\varepsilon$-$1/\varepsilon_m$) and ln(T-T_m) has a slope of $\gamma = 1.798$, indicating a typical feature of DPT behavior in the PLZT ceramics.

B. Electric field-induced transform

The relaxor ferroelectrics exhibit either an ergodic (ER) or a nonergodic (NE) state, which display different electric field-related properties. After being poled under an external electric field, the NE state can irreversibly transform into a stable long-range ferroelectric order, while the ER state reversibly returns from the electric field-induced ferroelectric state to the original ER state when the electric field is removed [33,34]. Raman spectroscopy, which is an efficient way to study the lattice vibrating modes and the structure modifications, can be carried out on the poled and unpoled PLZT ceramics to distinguish the ER or NE state. In lead-based ferroelectric perovskite materials, Raman spectroscopy can probe three main regions corresponding to different lattice vibrations: the low wavenumber region ($<$200 cm^{-1}) for vibrations of perovskite A-site, the middle wavenumber region (200–400 cm^{-1}) for B - O stretching vibrations, and the high wavenumber region ($>$400 cm^{-1}) for breathing and stretching modes of $\mathrm{BO_6}$ octahedra [35]. As shown in Fig. 2(a), within the high wavenumber region, the Raman phonon modes at about 415 and 680 cm^{-1} are more salient for the poled sample, which are assigned to the E(3TO) and E(4LO) phonon modes, respectively [36]. This indicates that the PLZT ceramic is in a NE state, and undergoes an electric field-induced irreversible transformation at room temperature.

Figure 2(b) compares the temperature dependence of permittivity and loss tangent for the unpoled and poled ceramics at 100 kHz during the heating process. Both permittivity curves show a maximum at the same temperature of 133 °C, indicating a similar temperature-induced phase transition. At low temperatures, an additional discontinuous anomaly of permittivity and a sharp peak

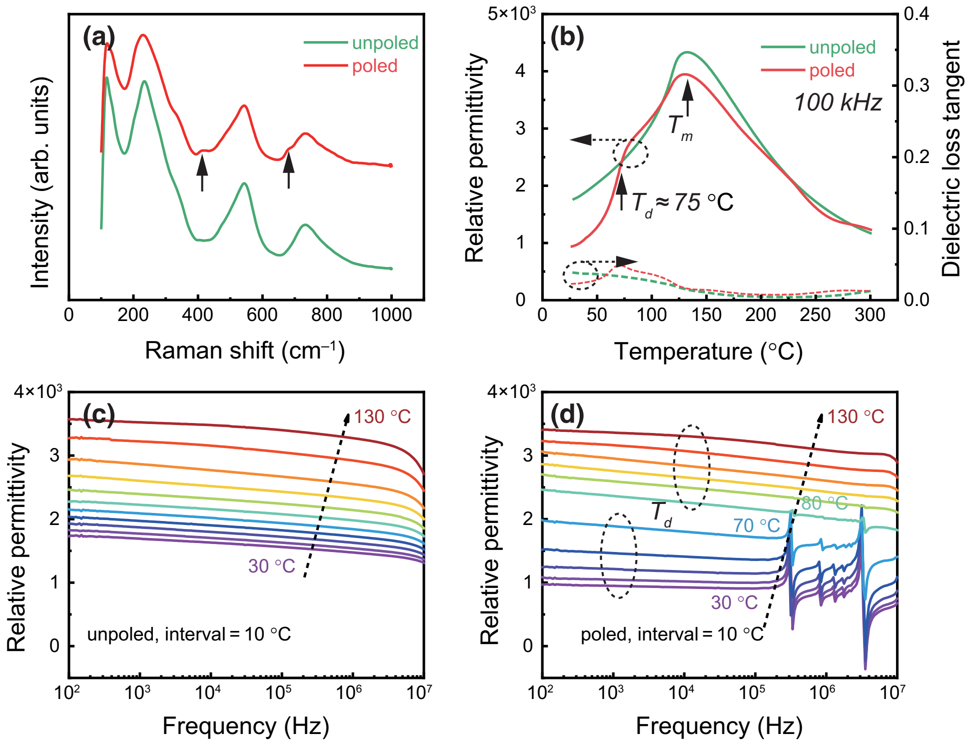

FIG. 2. (a) Raman spectra of unpoled and poled ceramics. (b) Temperature-dependent relative permittivity and loss tangent for unpoled and poled ceramics. Frequency-dependent relative permittivity under different temperatures for (c) unpoled and (b) poled ceramics.

of loss tangent emerge around 70 °C. Moreover, Figs. 2(c) and 2(d) show the frequency dependence of permittivity for different temperatures for the unpoled and poled ceramics. The frequency dependence of dielectric loss can be found in Fig. S2 (see Supplemental Material) [37]. The poled ceramic exhibits certain dielectric resonance above 2×10^5 Hz from room temperature to 70 °C, which disappears above 80 °C. This is similar to that in $BaTiO_3$ ferroelectric ceramics [38]. The dielectric resonance is related to macroscopic piezoelectricity, which is only found in the poled ferroelectrics with switchable domains oriented with external electric fields. Once the domains arrange entirely as disordered or crushed, the macroscopic piezoelectricity will disappear, as does the dielectric resonance phenomenon. For comparison, there is no dielectric anomaly for the unpoled ceramic in the whole temperature range. The difference between the poled and unpoled PLZT ceramics in dielectric frequency or temperature spectra was also found in $(Bi_{0.5}Na_{0.5})TiO_3$-$0.06BaTiO_3$ ceramics [39]. The phenomenon indicates that the thermal agitation makes the electric field-induced polar ferroelectric phase unstable and returns it to the nonpolar relaxor state, where the transition temperature is the depolarization temperature(T_d).

C. Ferroelectric behavior

Figures 3(a)–3(e) show the *P*-*E* and *I*-*E* loops measured at different temperatures. The ceramic has a typical ferroelectric hysteresis loop at 30 °C, which maintains the shape of a single loop up to 60 °C. Accordingly, the *I*-*E* loop shows two peaks of polarization switching current at the coercive fields ($\pm E_c$). When the temperature rises to 90 °C, a pinched *P*-*E* hysteresis loop occurs, and the current peaks split into four peaks ($\pm E_F$ and $\pm E_B$). The pinched loop is different from the double hysteresis loop in antiferroelectrics because the curve has a relatively high slope between 0 and $\pm E_F$ [40]. The strong pinning effect of defect dipoles on domain walls is eliminated in the ferroelectric hysteresis loop at different frequencies (Supplemental Material, Fig. S3) [37,41]. This is related to the electric field-induced reversible pseudo-first-order phase transition in relaxors, where the material is poled from the short-range-ordered ER state to the long-range-ordered ferroelectric phase at $\pm E_F$, and is depoled when the electric field is reduced to $\pm E_B$. With a further increase in temperature, the *P*-*E* loop gradually becomes narrower, accompanied by a smaller peak intensity in the *I*-*E* loop at 120 °C, indicating that the electric field-induced transition gradually turns to a second-order phase transition. Finally, we obtain a slim *P*-*E* loop and no peak is observed in the *I*-*E* curve, indicating a more stable nonpolar characteristic and greater difficulty in transforming into the ferroelectric phase. Figure 3(f) shows the temperature dependence of polarization (*P*-*T*) under different external electric fields from 0 to 40 kV/cm obtained from the upper branches of the *P*-*E* loops. The *P*-*T* curve under zero field shows a drastic drop near T_d, demonstrating the depolarization process. With increasing electric field, the change or jump in polarization gradually decreases to zero, signifying the phase transition from first order to second order.

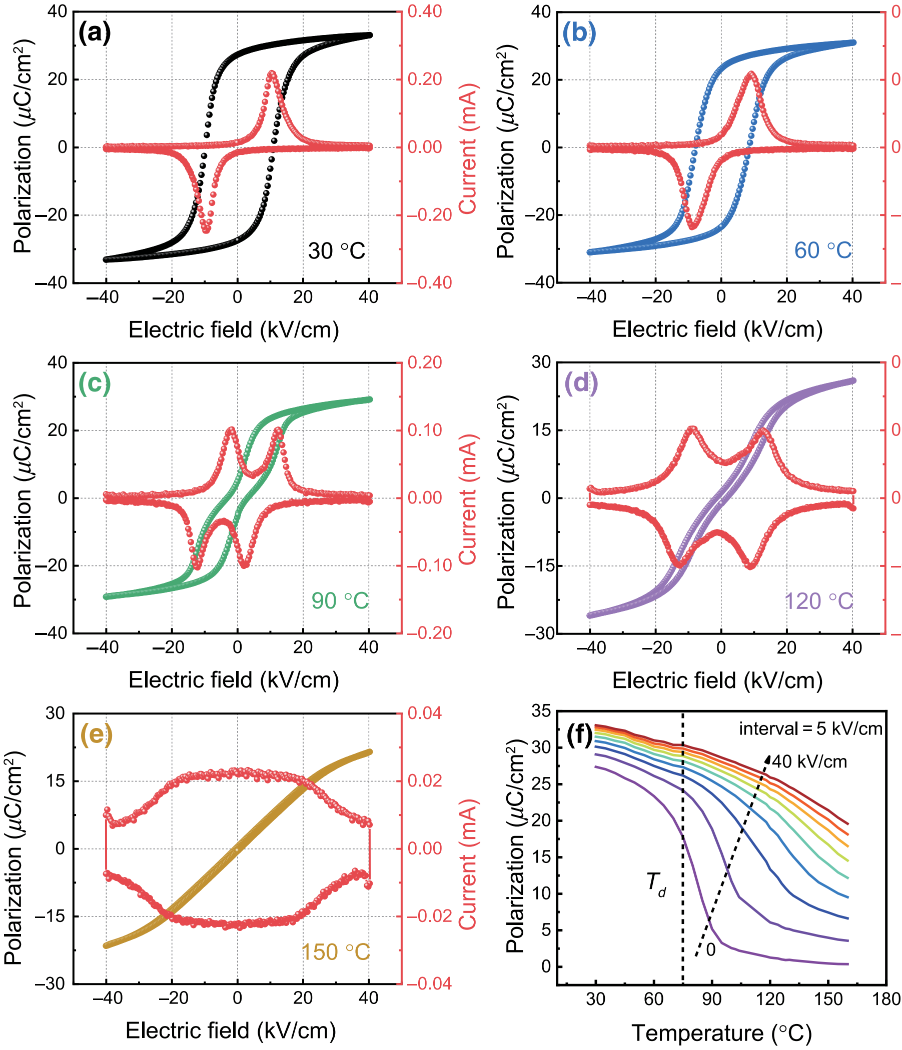

FIG. 3. (a)-(e) Ferroelectric hysteresis loops and corresponding current changes at different temperatures from 30ºC to 150 °C under $E = 40$ kV/cm and 1 Hz frequency. (f) Polarization intensity as a function of temperature for different electric fields.

D. Electrocaloric performance

Figure 4(a) presents a typical isothermal heat flow curve at 140 °C in the thermal equilibrium state under an electric field excitation of a square waveform (0–40 kV/cm). The application of an electric field leads to an exothermic peak, indicating that the sample releases heat. After the curve returns strictly to the equilibrium baseline, an endothermic response is induced by the removal of the field, demonstrating that the sample absorbs heat from the environment. In order to reduce experimental error, the cycle is repeated four times for each electric field, as shown in Fig. 4(b). The released and absorbed heats (ΔQ) have similar magnitudes, obtained by integrating the area under the exothermic and endothermic peaks, confirming that the joule heat is negligible in the measurements and the obtained ECE is reversible. The quantitative value of ΔT is obtained from the following equation

$$\Delta T = \frac{\Delta Q}{K \cdot c_p}, \qquad (3)$$

where c_p is the specific heat capacity obtained from Fig. 1(a) and K is the error factor (0.85, see Supplemental Material) [37]. The direct measurement ECE results for different temperatures and electric fields are shown in Fig. 4(c). Under a small electric field of 5 kV/cm, ΔT shows a peak (noted as Peak 1) near 70 °C, which gradually approaches zero when the temperature exceeds 100 °C. A stronger electric field of 10 kV/cm shifts the peak to a higher temperature of 80 °C, while another peak (noted as Peak 2) starts to appear near 125 °C. When the electric field reaches 20 kV/cm, Peak 2 is significantly enhanced, while there is a "platform" connecting the two peaks. When the electric field further increases to 30 kV/cm, Peak 2 moves to 130 °C and its value exceeds that of Peak 1. The ECE reaches a maximum of 0.98 K at 140 °C under 40 kV/cm. For comparison, Fig. 4(d) depicts the ECE calculated by the Maxwell relation [1,12]

$$\Delta T = -\frac{T}{\rho \cdot c_p} \int_{E_1}^{E_2} \left(\frac{\partial P}{\partial T}\right)_E dE, \qquad (4)$$

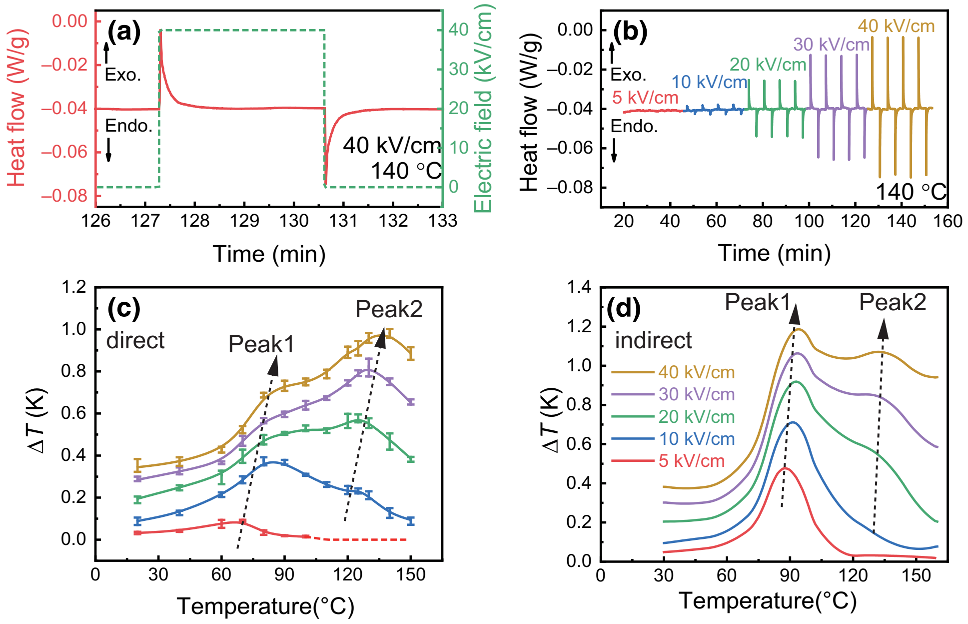

FIG. 4. (a) Typical isothermal heat flow changes with electric field of 40 kV/cm applied and removed at 140 °C. (b) Isothermal heat flow curves at 140 °C under different electric fields from 5 to 40 kV/cm. Temperature dependence of ΔT under different electric fields ($E_1 = 0$) by (c) direct isothermal heat flow measurement and (d) indirect Maxwell calculations.

where E_1 and E_2 represent the initial and final applied electric fields, respectively; $\partial P/\partial T$ is the pyroelectric coefficient, which is derived from the numerical differentiation of P-T curves [Fig. 3(f)]. There is a significant discrepancy between the two measurements despite the fact that the indirect results also exhibit double peaks.

Figures 5(a) and 5(b) compare the direct and indirect ECE results for the two peaks under different electric fields. These figures show negligible discrepancy in ΔT for Peak 2, but significant differences (approximately 0.4 K) for Peak 1. The differences between the indirect and direct measured values of ΔT for the two peaks are shown in Fig. 5(c). Figure 5(d) further compares the temperatures of the peak positions. For Peak 1, the temperature difference is as large as 20 °C under low electric fields, which gradually drops with increasing electric field. For Peak 2, the discrepancy is smaller and is quite insignificant for small fields. Our comparative analysis based on the peak values and positions, which we discuss below, suggests that the difference between the indirect and direct results for Peak 1 is primarily due to physical processes dominating under low electric fields.

In order to explore the mechanisms underlying the ECE evolution in relaxor ferroelectrics and explain the errors

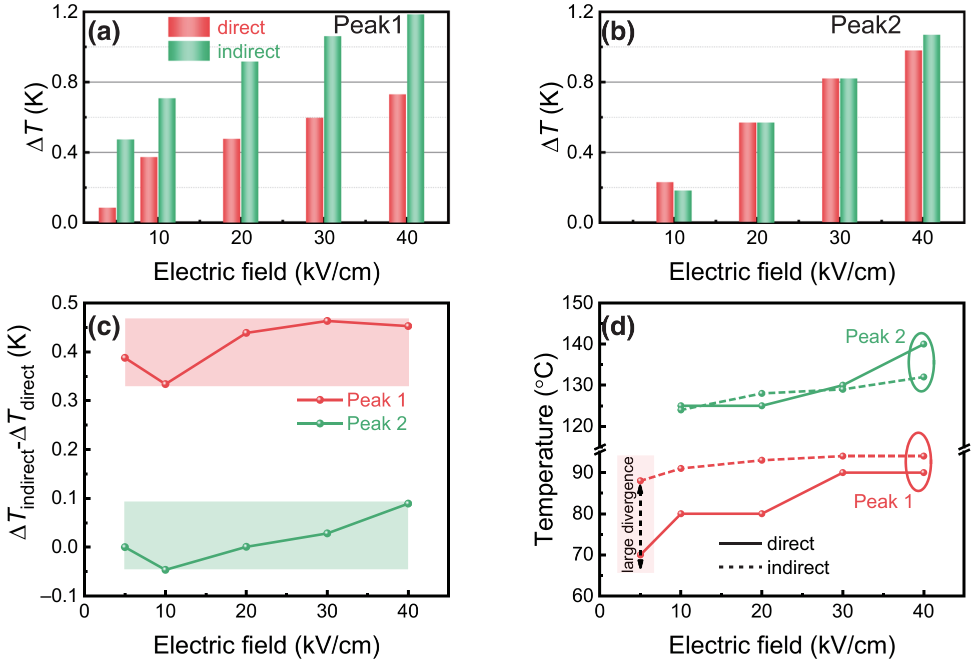

FIG. 5. Comparison of the direct and indirect ΔT under different electric fields for (a) Peak 1 and (b) Peak 2. (c) The difference in values between indirect and direct ΔT for Peak1 and Peak 2. (d) The temperatures associated with peak positions for direct and indirect ECE for Peak 1 and Peak 2.

due to the indirect thermodynamic calculation, a contour map of polarization switching current as a function of electric field and temperature is plotted in Fig. 6(a). The data is extracted from the absolute values from the lower branch of *I*-*E* loops [Figs. 3(a)–3(e)], where the electric field varies from 40 to −40 kV/cm. There are three temperature ranges separated by T_d and T_m, and the corresponding domain evolution processes are illustrated in Fig. 6(b). The substitutions La^{3+} for Pb^{2+} and Ti^{4+} for Zr^{4+} give rise to a disordered distribution of different ions at *A*/*B* sites of the perovskite lattice, thereby inducing local random fields. As $T < T_d$, the local random field is relatively weak so that the external electric field can irreversibly transform the PNRs into ferroelectric domains. Therefore, there is only one abnormal band, which represents the 180° macrodomain rotation for the poled samples or the transition from NE to ferroelectric state for the unpoled samples. However, this physical process is not involved in the direct ECE measurements, since no reverse field is applied. Therefore, only the non-180° macrodomain rotation contributes to the ECE entropy change. With increase in temperature, thermal agitation reduces the ordering of macrodomains and the entropy change is enhanced by the external electric field, as shown in Fig. 6(b). As $T_d < T < T_m$, the abnormal band branches, the macrodomains are destroyed, and PNRs are formed. Due to the disordering of thermally vibrating ions, the local random fields are relatively stronger and the formation of the ferroelectric polar state is prevented. Therefore, the weakly correlated PNRs are relatively stabilized under low electric fields and the small entropy change is the result of the orientations of the PNRs. With increasing temperature, the numbers and sizes of PNRs are reduced and the electric field-induced entropy change is now even smaller. This gives rise to a small ECE peak near T_d under 5 kV/cm, as shown in Fig. 4(c). Under a relatively high electric field, the local random fields can be overcome so that the PNRs are transformed into macrodomains accompanied by a large ECE ΔT. In contrast to the behavior for fields below 5 kV/cm, the ECE ΔT continues to increase with increasing temperature under an electric field

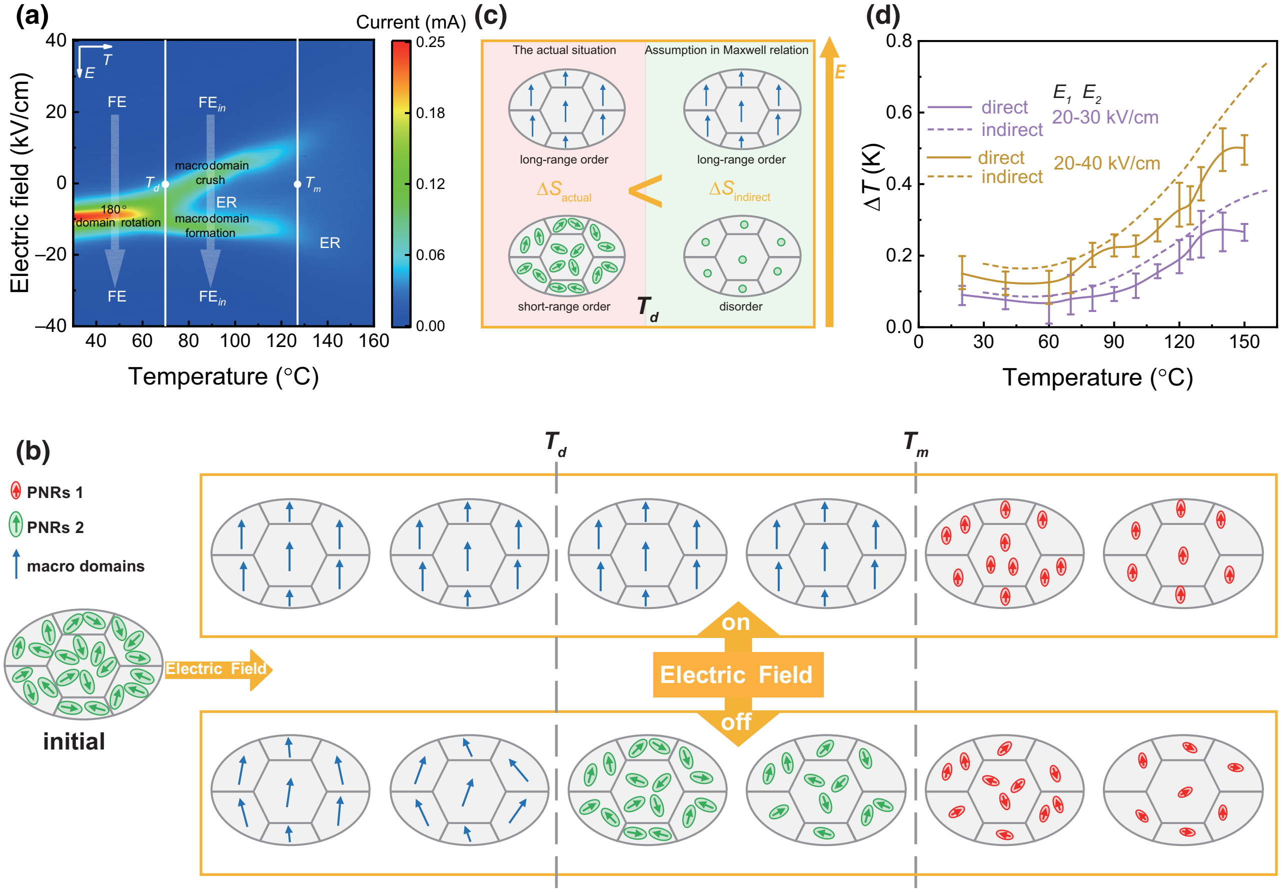

FIG. 6. (a) Contour plots of the *I*-*E* loops from Fig. 3 as a function of temperature. (b) Schematic illustration of the domain evolution processes for PLZT relaxor ceramics under coupling of electric field and temperature. (c) A comparison of the actual situation near T_d in which PNRs contribute to the dipole order entropy with the Maxwell relation, which assumes a paraelectric phase. Thus, the electric field-induced actual entropy change near T_d is smaller than predicted using the Maxwell calculation. (d) Temperature dependence of ΔT ($E_1 = 20$ kV/cm, $E_2 = 30$ kV/cm, and 40 kV/cm) by direct isothermal heat flow measurement and indirect Maxwell calculation.

greater than 20 kV/cm, and forms a “platform” of large ECE ΔT between T_d and T_m since the transition is a continuous and gradual process, as illustrated in Fig. 6(b). The 10 kV/cm is a critical electric field, where some of the PNRs transform into macrodomains.

There is no consensus yet in the literature on an understanding of T_m. Some studies suggest that the PNRs are highly dynamic under thermal agitation above T_m, where the electric dipole moment is a function of both time and position. When the temperature is below T_m, the PNRs with various polarization directions are frozen and static but are evenly distributed across the grains, that is, they keep a neutral macroscopic polarization [34,42–44]. Other studies maintain that the T_m is associated with a phase transition for PNRs from dynamic to frozen [45–48]. Nevertheless, both emphasize that PNRs have different properties below or above T_m. As shown in Fig. 6(b), PNRs for $T < T_m$ are noted as PNRs 1, and for $T > T_m$ are noted as PNRs 2. With an increase in temperature, PNRs become smaller in size and fewer in number. Different from PNRs 1, the PNRs 2, which are smaller and fewer, are more difficult to transform into macrodomains due to the extremely strong local random fields. In fact, the properties of relaxors above T_m are close to those of the paraelectric phase where the frequency dispersion disappears, as shown in Fig. 1(b). Therefore, the PLZT relaxor shows another ECE peak near T_m under relatively high electric fields. In addition, the DPT in Fig. 1(a) reflects the transition of overall phase structure near T_m, which also contributes to the ECE Peak 2.

The discrepancy between direct and indirect results mainly depends on the enhanced ΔT near T_d, where the macroscopic polarization changes. In other words, the ER state, where the numerous PNRs also contribute to the dipole order entropy, is mistaken for the paraelectric phase by the Maxwell relation [see Fig. 6(c)]. Therefore, the electric field-induced actual entropy changes near T_d are smaller than those obtained from the indirect calculation. Interestingly, when the initial electric field E_1 exceeds 20 kV/cm (within the temperature range below T_m), only the evolution of macrodomains contributes to the ECE ΔT. In this case, the results of the direct and indirect methods are consistent below T_m, as shown in Fig. 6(d). This shows that the Maxwell relation does not incorporate the changes and evolution associated with the PNRs.

Finally, our results also have a bearing on ECE materials’ design. Our work indicates that an ECE peak can be induced not only by a structural phase transition, but also via the transitions between short-range PNRs and the long-range ferroelectric phase or even by two kinds of PNRs. For PNRs, we have seen that the ΔT-T curves possess a “platform” between the two peaks at T_d and T_m. This means that a large electrocaloric ΔT can be obtained over a broad temperature range. This is highly desirable for cooling applications as it suggests we can design ECE materials by using relaxor ferroelectrics with a large T_m-T_d.

IV. CONCLUSIONS

In summary, the ECEs in PLZT relaxor ceramics, which are studied by direct isothermal heat flow measurements, demonstrate double-peak ΔT-T curves. The low-temperature peak has a $\Delta T_{\max} = 0.7$ K (80 °C, 40 kV/cm) and responds to the transition from long-range ferroelectric order to short-range order involving PNRs. The high-temperature peak shows a $\Delta T_{\max} = 0.98$ K (140 °C, 40 kV/cm) related to the transition between two kinds of PNRs with different phase structures or motion states. In addition, the electrocaloric evolution in a temperature range below T_m mainly depends on three physical processes: the ordering of PNRs, the formation of macroscopic ferroelectric domains from PNRs, and the ordering of ferroelectric domains. The first two are not incorporated in the electrocaloric calculation based on the Maxwell relation that assumes equilibrium. This is the main reason for the significant differences between direct and indirect measurement methods, especially near T_d. Our work also suggests how we can design relaxor ferroelectric ceramics with large ECE over a broad temperature range by exploiting the transitions between PNRs.

ACKNOWLEDGMENTS

This work was supported by grants from the National Natural Science Foundation of China (Grants No. 51741202 and No. 51372018) and National Key Research and Development Program of China (Grant No. 2018YFB0704301).

[1] A. S. Mischenko, Q. Zhang, J. F. Scott, R. W. Whatmore, and N. D. Mathur, Giant electrocaloric effect in thin-film $PbZr_{0.95}Ti_{0.05}O_3$, Science **311**, 1270 (2006).

[2] B. Neese, B. Chu, S. Lu, Y. Wang, E. Furman, and Q. M. Zhang, Large electrocaloric effect in ferroelectric polymers near room temperature, Science **321**, 821 (2008).

[3] R. Ma, Z. Zhang, K. Tong, D. Huber, R. Kornbluh, Y. S. Ju, and Q. Pei, Highly efficient electrocaloric cooling with electrostatic actuation, Science **357**, 1130 (2017).

[4] J. F. Scott, Applications of modern ferroelectrics, Science **315**, 954 (2007).

[5] M. Valant, Electrocaloric materials for future solid-state refrigeration technologies, Prog. Mater. Sci. **57**, 980 (2012).

[6] J. Wu, *Advances in Lead-free Piezoelectric Materials* (Springer, Inc., Singapore, 2018).

[7] H. Huang and J. F. Scott, *Ferroelectric Materials for Energy Applications* (John Wiley & Sons, Weinheim, 2018).

[8] X. Moya, E. Stern Taulats, S. Crossley, D. González Alonso, S. Kar Narayan, A. Planes, L. Mañosa, and N.

D. Mathur, Giant electrocaloric strength in single-crystal $BaTiO_3$, Adv. Mater. **25**, 1360 (2013).

[9] J. Li, S. Qin, Y. Bai, J. Li, and L. Qiao, Flexible control of positive and negative electrocaloric effects under multiple fields for a giant improvement of cooling capacity, Appl. Phys. Lett. **111**, 93901 (2017).

[10] Y. Bai, D. Wei, and L. Qiao, Control multiple electrocaloric effect peak in $Pb(Mg_{1/3}Nb_{2/3})O_3$-$PbTiO_3$ by phase composition and crystal orientation, Appl. Phys. Lett. **107**, 192904 (2015).

[11] F. Han, Y. Bai, L. Qiao, and D. Guo, A systematic modification of the large electrocaloric effect within a broad temperature range in rare-earth doped $BaTiO_3$ ceramics, J. Mater. Chem. C **4**, 1842 (2016).

[12] J. Li, Y. Bai, S. Qin, J. Fu, R. Zuo, and L. Qiao, Direct and indirect characterization of electrocaloric effect in $(Na,K)NbO_3$ based lead-free ceramics, Appl. Phys. Lett. **109**, 954 (2016).

[13] X. S. Qian, H. J. Ye, Y. T. Zhang, H. Gu, X. Li, C. A. Randall, and Q. M. Zhang, Giant electrocaloric response over a broad temperature range in modified $BaTiO_3$ ceramics, Adv. Funct. Mater. **24**, 1300 (2014).

[14] Y. Bai, G. Zheng, K. Ding, L. Qiao, S. Shi, and D. Guo, The giant electrocaloric effect and high effective cooling power near room temperature for $BaTiO_3$ thick film, J. Appl. Phys. **110**, 94103 (2011).

[15] X. Jian, B. Lu, D. Li, Y. Yao, T. Tao, B. Liang, and S. Lu, Large electrocaloric effect in lead-free $Ba(Zr_xTi_{1-x})O_3$ thick film ceramics, J. Alloy. Compd. **742**, 165 (2018).

[16] L. Fulanović, S. Drnovšek, H. Uršič, M. Vrabelj, D. Kuščer, K. Makarovič, V. Bobnar, Z. Kutnjak, and B. Malič, Multilayer $0.9Pb(Mg_{1/3}Nb_{2/3})O_3$-$0.1PbTiO_3$ elements for electrocaloric cooling, J. Eur. Ceram. Soc. **37**, 599 (2017).

[17] B. Peng, H. Fan, and Q. Zhang, A giant electrocaloric effect in nanoscale antiferroelectric and ferroelectric phases coexisting in a relaxor $Pb_{0.8}Ba_{0.2}ZrO_3$ thin film at room temperature, Adv. Funct. Mater. **23**, 2987 (2013).

[18] Y. Zhao, X. Hao, and Q. Zhang, A giant electrocaloric effect of a $Pb_{0.97}La_{0.02}(Zr_{0.75}Sn_{0.18}Ti_{0.07})O_3$ antiferroelectric thick film at room temperature, J. Mater. Chem. C **3**, 1694 (2015).

[19] B. Peng, Q. Zhang, Y. Lyu, L. Liu, X. Lou, C. Shaw, H. Huang, and Z. Wang, Thermal strain induced large electrocaloric effect of relaxor thin film on $LaNiO_3/Pt$ composite electrode with the coexistence of nanoscale antiferroelectric and ferroelectric phases in a broad temperature range, Nano Energy **47**, 285 (2018).

[20] B. Lu, P. Li, Z. Tang, Y. Yao, X. Gao, W. Kleemann, and S. Lu, Large electrocaloric effect in relaxor ferroelectric and antiferroelectric lanthanum doped lead zirconate titanate ceramics, Sci. Rep. **7**, 45335 (2017).

[21] J. Li, D. Zhang, S. Qin, T. Li, M. Wu, D. Wang, Y. Bai, and X. Lou, Large room-temperature electrocaloric effect in lead-free $BaHf_xTi_{1-x}O_3$ ceramics under low electric field, Acta Mater. **115**, 58 (2016).

[22] Y. Bai, X. Han, K. Ding, and L. Qiao, Combined effects of diffuse phase transition and microstructure on the electrocaloric effect in $Ba_{1-x}Sr_xTiO_3$ ceramics, Appl. Phys. Lett. **103**, 162902 (2013).

[23] X. Jian, B. Lu, D. Li, Y. Yao, T. Tao, B. Liang, J. Guo, Y. Zeng, J. Chen, and S. Lu, Direct measurement of large electrocaloric effect in $Ba(Zr_xTi_{1-x})O_3$ ceramics, ACS Appl. Mater. Interfaces **10**, 4801 (2018).

[24] A. Axelsson, F. Le Goupil, M. Valant, and N. M. Alford, Electrocaloric effect in lead-free Aurivillius relaxor ferroelectric ceramics, Acta Mater. **124**, 120 (2017).

[25] S. G. Lu, B. Rožič, Q. M. Zhang, Z. Kutnjak, R. Pirc, M. Lin, X. Li, and L. Gorny, Comparison of directly and indirectly measured electrocaloric effect in relaxor ferroelectric polymers, Appl. Phys. Lett. **97**, 202901 (2010).

[26] M. Sanlialp, V. V. Shvartsman, M. Acosta, B. Dkhil, and D. C. Lupascu, Strong electrocaloric effect in lead-free $0.65Ba(Zr_{0.2}Ti_{0.8})O_3$-$0.35(Ba_{0.7}Ca_{0.3})TiO_3$ ceramics obtained by direct measurements, Appl. Phys. Lett. **106**, 62901 (2015).

[27] F. Li, G. Chen, X. Liu, J. Zhai, B. Shen, S. Li, P. Li, K. Yang, H. Zeng, and H. Yan, Type-I pseudo-first-order phase transition induced electrocaloric effect in lead-free $Bi_{0.5}Na_{0.5}TiO_3$-$0.06BaTiO_3$ ceramics, Appl. Phys. Lett. **110**, 182904 (2017).

[28] G. Chen, Y. Zhang, X. Chu, G. Zhao, F. Li, J. Zhai, Q. Ren, B. Li, and S. Li, Large electrocaloric effect in La-doped $0.88Pb(Mg_{1/3}Nb_{2/3})O_3$-$0.12PbTiO_3$ relaxor ferroelectric ceramics, J. Alloy. Compd. **727**, 785 (2017).

[29] M. M. Vopson, G. Caruntu, and X. Tan, Polarization reversal and memory effect in anti-ferroelectric materials, Scr. Mater. **128**, 61 (2017).

[30] Z. Xu, Z. Fan, X. Liu, and X. Tan, Impact of phase transition sequence on the electrocaloric effect in $Pb(Nb,Zr,Sn,Ti)O_3$ ceramics, Appl. Phys. Lett. **110**, 82901 (2017).

[31] X. G. Tang, K. Chew, and H. Chan, Diffuse phase transition and dielectric tunability of $Ba(ZryTi_{1-y})O_3$ relaxor ferroelectric ceramics, Acta Mater. **52**, 5177 (2004).

[32] W. Cai, C. Fu, J. Gao, Z. Lin, and X. Deng, Effect of hafnium on the microstructure, dielectric and ferroelectric properties of $Ba[Zr_{0.2}Ti_{0.8}]O_3$ ceramics, Ceram. Int. **38**, 3367 (2012).

[33] F. Weyland, M. Acosta, J. Koruza, P. Breckner, J. Rödel, and N. Novak, Criticality: Concept to enhance the piezoelectric and electrocaloric properties of ferroelectrics, Adv. Funct. Mater. **26**, 7326 (2016).

[34] A. A. Bokov and Z. G. Ye, Recent progress in relaxor ferroelectrics with perovskite structure, J. Mater. Sci. **41**, 31 (2006).

[35] K. Jiang, P. Zhang, J. Zhang, G. Xu, W. Li, Z. Hu, and J. Chu, Relationship between negative thermal expansion and lattice dynamics in a tetragonal $PbTiO_3$-$Bi(Mg_{1/2}Ti_{1/2})O_3$ perovskite single crystal, RSC Adv. **6**, 3159 (2016).

[36] F. Yang, X. Cheng, Z. Zhou, and Y. Zhang, An analysis of domain reorientation in PLZT ceramics by in situ Raman spectroscopy, J. Appl. Phys. **106**, 114115 (2009).

[37] See Supplemental Material at http://link.aps.org/supplemental/10.1103/PhysRevApplied.11.044032 for details of phase composition, microstructure, more dielectric and ferroelectric data, and the calibrations of modified DSC for direct ECE measurement.

[38] Y. Feng, W. Li, D. Xu, Y. Qiao, Y. Yu, Y. Zhao, and W. Fei, Defect engineering of Lead-free piezoelectrics

with high piezoelectric properties and temperature-stability, ACS Appl. Mater. Interfaces **8**, 9231 (2016).

[39] J. Zhao, N. Zhang, W. Ren, G. Niu, D. Walker, P. A. Thomas, L. Wang, and Z. Ye, Polar domain structural evolution under electric field and temperature in the $(Bi_{0.5}Na_{0.5})TiO_3$-0.06$BaTiO_3$ piezoceramics, J. Am. Ceram. Soc. **102**, 437 (2019).

[40] M. M. Vopson and X. Tan, Nonequilibrium polarization dynamics in antiferroelectrics, Phys. Rev. B **96**, 14104 (2017).

[41] X. Cao, H. Tian, C. Hu, Y. Wang, X. Li, L. Li, X. Sun, and Z. Zhou, Discovery and evolution of double P-E loops in a tetragonal Fe-doped $KTa_{0.57}Nb_{0.43}O_3$ single crystal, J. Am. Ceram. Soc. **101**, 3755 (2018).

[42] X. Yao, Z. Chen, and L. E. Cross, Polarization and depolarization behavior of hot pressed lead lanthanum zirconate titanate ceramics, J. Appl. Phys. **54**, 3399 (1983).

[43] A. A. Bokov, Ferroelectric domains and polar clusters in disordered structures, Ferroelectrics **190**, 197 (1997).

[44] W. A. Chang, C. H. Hong, B. Y. Choi, H. P. Kim, H. S. Han, Y. Hwang, W. Jo, K. Wang, J. F. Li, and J. S. Lee, A brief review on relaxor ferroelectrics and selected issues in lead-free relaxors, J. Korean Phys. Soc. **68**, 1481 (2016).

[45] X. Liu, J. Zhai, and B. Shen, Local phenomena in bismuth sodium titanate perovskite studied by Raman spectroscopy, J. Am. Ceram. Soc. **101**, 5604 (2018).

[46] W. Jo, S. Schaab, E. Sapper, L. A. Schmitt, H. Kleebe, A. J. Bell, and J. Rödel, On the phase identity and its thermal evolution of lead free $(Bi_{1/2}Na_{1/2})TiO_3$-6mol% $BaTiO_3$, J. Appl. Phys. **110**, 74106 (2011).

[47] W. Jo, R. Dittmer, M. Acosta, J. Zang, C. Groh, E. Sapper, K. Wang, and J. Rödel, Giant electric-field-induced strains in lead-free ceramics for actuator applications-status and perspective, J. Electroceram. **29**, 71 (2012).

[48] X. Liu, J. Zhai, B. Shen, F. Li, Y. Zhang, P. Li, and B. Liu, Study of temperature-induced structural evolution in $(Na_{0.5}Bi_{0.5})TiO_3$-$(K_{0.5}Bi_{0.5})TiO_3$-$(K_{0.5}Na_{0.5})NbO_3$ lead-free ceramics, Curr. Appl. Phys. **17**, 774 (2017).